Earth and Space Science

RESEARCH ARTICLE
10.1029/2019EA000670

Calibration of the Heat Flow and Physical Properties Package (HP^3) for the InSight Mars Mission

M. Grott[1], T. Spohn[1], J. Knollenberg[1], C. Krause[2], M. Scharringhausen[3], T. Wippermann[3], S.E. Smrekar[4], T.L. Hudson[4], and W.B. Banerdt[4]

[1]Institute of Planetary Research, German Aerospace Center (DLR), Berlin, Germany, [2]Space Operations and Astronaut Training, German Aerospace Center (DLR), Cologne, Germany, [3]Institute of Space Systems, German Aerospace Center (DLR), Bremen, Germany, [4]Jet Propulsion Laboratory, California Institute of Technology, Pasadena, CA, USA

Abstract The (HP^3) of the InSight Mars mission is an instrument package to measure the Martian geothermal heat flow. The instrument's platinum resistance temperature sensors have been calibrated between −75 and +55 °C, and the absolute temperature uncertainty of the calibration is 10 mK. Temperature differences can be measured with an uncertainty of better than 5 mK. HP^3 determines regolith thermal conductivity by using the HP^3 mole as a modified line heat source, and thermal conductivity can be measured with an uncertainty of better than 4%. Tilt sensors used to determine the attitude of the mole during penetration measure tilt with an uncertainty of better than 0.25°.

Key Points:
- The Heat Flow and Physical Properties Package (HP^3) of the InSight Mars mission is a heat flow probe designed to measure the temperature gradient and thermal conductivity of the Martian regolith to a depth of 5 m
- To reconstruct sensor depth, tiltmeters measure the emplacement angle with an uncertainty of better than 0.25°
- Temperature sensors have been calibrated to measure temperature difference with an uncertainty of better than 5 mK; thermal conductivity can be measured with an uncertainty of better than 4%; all stated uncertainties are 1σ confidence limits

Correspondence to:
M. Grott,
matthias.grott@dlr.de

Citation:
Grott, M., Spohn, T., Knollenberg, J., Krause, C., Scharringhausen, M., Wippermann, T., et al. (2019). Calibration of the heat flow and physical properties package (HP^3) for the InSight Mars mission. *Earth and Space Science*, *6*, 2556–2574. https://doi.org/10.1029/2019EA000670

Received 12 APR 2019
Accepted 29 NOV 2019
Accepted article online 11 DEC 2019
Published online 28 DEC 2019

1. Introduction

Surface heat flow is a fundamental parameter that quantifies the amount of heat lost from a planetary interior. It is routinely measured in deep wells on Earth's continents, as well as in sediments on the ocean floor (Davies & Davies, 2010; Davies, 2013), and more than 38,000 terrestrial heat flow measurements have been performed (Davies, 2013). The collected data indicates a total heat loss of 44–47 TW from the Earth's interior (Davies, 2013; Jaupart & Mareschal, 2015; Pollack et al., 1993), corresponding to an average surface heat flow of 86 mW m^{-2}. Heat flow is largest at divergent plate boundaries, and the mean oceanic heat flow is 95.9 mW m^{-2}, significantly larger than the mean continental heat flow of 64.7 mW m^{-2} (Davies, 2013).

Except for the Earth, heat flow measurements have so far only been attempted on the Moon, and successful heat flow measurements have been performed during the Apollo 15 and 17 missions (Langseth et al., 1972a, 1976). At the time, average heat flow from the Moon was estimated to be 18 mW m^{-2} (Langseth et al., 1976), but corrections later applied by Warren and Rasmussen (1987) reduced this value to 12 mW m^{-2}. This indicates a lunar bulk concentration of heat producing elements similar to that of the Earth. Heat flow from other bodies in the solar system has so far only been estimated indirectly, and the current knowledge of the martian planetary heat flow has been summarized by, for example, Grott et al. (2013) and Ruiz (2014). Present-day Martian heat flow is estimated to be 14–25 mW m^{-2} (Plesa et al., 2015, 2018; Parro et al., 2017; Smrekar et al., 2019), in between the lunar and terrestrial values.

The InSight Mars mission (Banerdt et al., 2012), which landed on 26 November 2018, installed a geophysical station at its landing site in Elysium Planitia (Golombek et al., 2017). One of InSight's payloads is the Heat Flow and Physical Properties Package (HP^3) (Spohn et al., 2018), which will attempt the first direct measurement of the Martian planetary heat flow. To determine heat flow, the near surface temperature gradient as well as the thermal conductivity of the regolith need to be measured, and HP^3 will achieve this by emplacing 14 temperature sensors mounted on a 5-m-long tether towed behind a self-hammering penetrator (compare Figure 8 of Spohn et al., 2018). During descent, depth of the sensors will be determined by measuring the attitude of the mole with respect to vertical using static tiltmeters, while simultaneously measuring the amount of paid-out tether. Furthermore, the thermal conductivity of the regolith will be determined at 50-cm depth intervals using the mole as a modified line heat source (LHS) (Hammerschmidt & Sabuga, 2000a). Details of the design of the heat flow probe are given in Spohn et al. (2018).

In this paper, we will describe the calibration of the HP^3 sensors starting with the calibration of the platinum resistance temperature detectors (PT100). Calibration and verification of the thermal conductivity

Table 1
Summary of Sensor Drift for Three Industrial Standard PT100 Sensors After Exposing Them to Different Test Environments

Test	IST wired	IST SMD	Jumo
Hysteresis	2.5 mK	12.5 mK	2.5 mK
Thermal cycling	<5 mK	<5 mK	<5 mK
Random vibration	<5 mK	9 mK	<5 mK
Pyro shock	<5 mK	13 mK	20 mK
Nusil CV-2946	<5 mK	<5 mK	30 mK
Nusil CV-1152	<5 mK	<5 mK	10 mK
Ecobond 285	100 mK	<5 mK	<5 mK

Note. The change detection threshold for the given calibration setup is 5 mK (1σ) and governed by the calibration bath inhomogeneity.

measurement will then be discussed. Finally, calibration of the tiltmeters will be described, and uncertainties will be given for all measurements. Taken together, the heat flow measurement uncertainty is expected to be better than 5% at a 1-σ level, but systematic errors caused by the measurement setup close to the InSight lander will likely increase this figure to 10% (Spohn et al., 2018). This is well within the required measurement uncertainty of ± 5 mW m^{-2} for the range of heat flow expected on Mars.

1.1. Choice of Temperature Sensors

Before starting the calibration of temperature senors, it is important to verify that sensors will not change characteristics when exposed to the harsh environment encountered during the mission. Therefore, temperature sensors on the tether have been carefully chosen and tested to guarantee that the ground calibration is applicable after exposing the sensors to the stresses of launch, landing, and Martian diurnal temperature cycles. This approach was comparable to that applied during the development of the Apollo heat flow probes (Langseth & Keihm, 1977). For the critical subsurface temperature measurements, three types of platinum based resistive temperature detectors have been tested for performance and stability under temperature, vibration, shock, and mechanical loads: (1) wired IST thin film sensors; (2) surface mount (SMD) IST thin film sensors; (3) Jumo Platinum wire sensors, glass potted.

For the mechanical tests, four units of each sensor type were soldered to a test printed circuit board (PCB), and the sensors on the board were then calibrated according to the procedure below (section 2.1). Prestress hysteresis of the sensors was determined by calibration and the board was then exposed to four thermal cycles between −75 and +55 °C followed again by sensor calibration. Subsequently, random vibrational loads of 53.2 g_{RMS} as well as pyroshock loads of 47, 2,370, and 2,370 g at 100, 2,000, and 1,0000 Hz were applied, respectively. After the tests, calibration was repeated and the drift of the sensors with respect to their pretest calibration was determined. Then, sensors were potted with different adhesives to study the influence of mechanical confinement on hysteresis and sensor performance. For these tests, three space qualified adhesives have been used: (1) Silicone adhesive Nusil CV-2946; (2) silicone adhesive Nusil CV-1152; (3) epoxy adhesive Eccobond 285. Again, after potting, a calibration of the sensors was performed and deviations from the previous calibration runs were determined.

Results of these tests are summarized in Table 1, where the temperature drift following the different tests is given. Using the calibration setup described below, temperature drift above 5 mK can be detected, and IST wired thin film sensors turned out to be most stable under the imposed conditions as long as epoxy adhesives are not used for potting. Therefore, as a result of these tests, IST wired thin film sensors were chosen for the HP^3 instrument, and sensors on the tether were coated with the Nusil CV-1152 silicone adhesive. The latter was chosen over the CV-2946, as it bonds better to the Kapton than CV-2946, which is easily sheared-off under mechanical loads.

2. Temperature Sensor Calibration

2.1. Calibration Setup and Procedure

The HP^3 subsystem measuring subsurface temperatures is termed TEM-P, where P refers to a passive thermal measurement as opposed to the active heating required for thermal conductivity determination

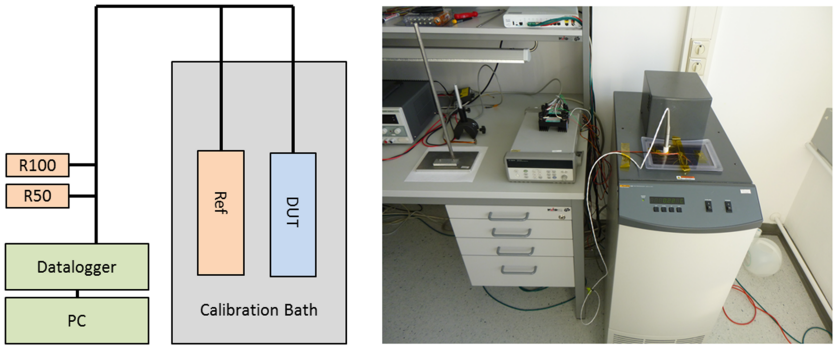

Figure 1. (left) Schematics of the setup for temperature calibration. The device under test (DUT, i.e., the TEM-P or TEM-A sensor assembly) is placed inside the calibration bath along with the reference thermometer, and data are read by a benchtop data logger and computer. Measurements are referenced to two calibrated reference resistors of 50 and 100 Ω. (right) Picture of the setup in the DLR thermal lab, with the calibration bath on the right hand side. The reference thermometer is immersed in the bath, while the reference resistors are located on top of the data logger.

(TEM-A, see below). TEM-P consists of 14 PT100 sensors, which are mounted on a Kapton based tether, and associated readout electronics, which measure the PT100 resistance in a four-wire (Kelvin) configuration (see Spohn et al., 2018, for a detailed description of the readout circuit). Prior to mounting the sensors on the tether, the PT100 reliability was tested by exposing them to 10 temperature cycles between −70 and +70 °C, followed by a burn-in test using a measurement current of 3 mA at +70 °C for 168 hr. In addition, a subset of nonflight sensors from the same lot were exposed to 1,000 hr at +150 °C using the same source current to identify manufacturing flaws. All sensors passed these tests. Calibration of the PT100 sensors was carried out after integration on the tether, which included potting the sensors for mechanical protection using silicone adhesive. Therefore, the sensor configuration during calibration was identical to that in the Mars application.

HP^3 measures thermal conductivity using the TEM-A sensors, which are capton-based copper heating foils integrated into the HP^3 mole's outer hull (see Spohn et al. (2018) for details). Due to the large temperature coefficient of resistance, the heating foils simultaneously act as sensing elements, and TEM-A sensors have been calibrated using the same setup as the one used for TEM-P. Prior to calibration, sensors have been temperature cycled 20 times between −70 and +55 °C to reduce sensor drift. Furthermore, high-temperature storage at 125° was carried out for 100 hr.

Temperature calibration of TEM-P and TEM-A was carried out in the thermal lab at DLR and consisted in a comparison calibration with a secondary standard Hart Scientific 5615 platinum reference thermometer (Ser. Nr. 824018). The calibration of the reference thermometer itself was verified using a triple point of water (273.1600 K) and a gallium (302.9146 K) fix point cell. Sensors and reference thermometers were simultaneously immersed in a thermal equilibration bath, and the schematic setup is illustrated in the left panel of Figure 1, while an image of the setup is shown in the right panel of the figure.

The equipment used for the calibration consisted of a Hart Scientific 7318 calibration bath, which guarantees homogeneous and stable temperatures across the bath to within 7 mK. The resistance of the device under test and the reference thermometer were measured using an Agilent 34907A data logger, which was equipped with two 34901A data logger modules for multiplexing the different signals. In addition to the sensor resistance, two reference resistors (Burster-1240 100-Ohm reference resistor, Ser. Nr. 562062, and Burster-1240 50-Ohm reference resistor, Ser. Nr. 561166) were simultaneously measured to correct for data logger offset and gain errors (see below).

Calibration of the sensors was performed at temperatures of 0, +20, +40, +55, +40, +20, 0, −20, −40, −60, −75, −60, −40, −20, and 0 °C, and temperatures were allowed to stabilize at each of the calibration points for 75 min. The temperature profile as used during instrument calibration is shown in Figure 2 where the temperature of the reference thermometer is shown as a function of time. In addition, the times used to read-off the resistance of the thermally equilibrated TEM-P and TEM-A sensors is indicated by red dots. Note that by following the above calibration sequence, hysteresis of the sensors can be quantified.

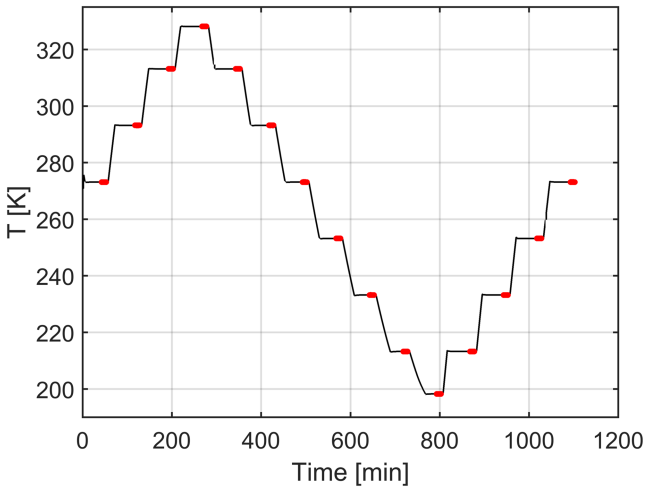

Figure 2. Temperature of the reference thermometer as a function of time during calibration. Temperatures are stabilized at the predefined set points to allow the DUT to attain an equilibrated thermal state. Measurements are evaluated at the end of the temperature plateaus, indicated in red, to obtain stable temperature readings.

For TEM-P, the calibration procedure then consisted of the following steps: (1) The tether was rolled tightly onto a mounting fixture and connected to the data logger; (2) the fixture including the tether was immersed into the calibration bath; (3) the reference thermometer and reference resistors were connected to the data logger; (4) the reference thermometer was immersed in the calibration bath; (5) data logging was started, and the bath temperature was set to the first calibration point; (6) data were taken for 75 min. (7) The above steps (5 and 6) were repeated for the remaining calibration points. After finishing the calibration, mounting fixture and reference thermometer were removed from the calibration bath and data were stored for later analysis.

In general, thermal equilibrium between calibration bath and reference thermometer was reached after 20 min for each calibration point (cf. Figure 2), but the TEM-P sensors reacted more slowly. This is due to the tether being mounted on the calibration fixture, and TEM-P sensors reach thermal equilibrium after 60 min as a maximum. To include some time margin, only the final 5 min of data (30 samples) for each 75-min equilibration interval were used for evaluating the sensor resistance at each calibration point, and these times are indicated in red in Figure 2. Measured resistance R_m as a function of temperature T for the individual TEM-P sensors was then obtained by simple arithmetic averaging of resistance readings during these time intervals.

For TEM-A, the same procedure as described above was implemented, but due to the mounting of the TEM-A sensors on the metallic mole outer hull, thermal coupling between calibration bath and device under test was much improved. Therefore, thermal equilibrium was reached earlier, but the total thermal equilibration time of 75 min was not changed to keep a robust time margin. Again, only the last 5 min of each temperature plateau were used to determine $R_m(T)$.

2.2. Calibration Data Evaluation

To reference the measured resistances R_m to known standards, the resistance readings $R_{m,50}$ and $R_{m,100}$ of the calibrated 50- and 100-Ω reference resistors were determined and averaged for the same time periods used for determining $R_m(T)$. Taking offset and gain errors into account, the measured resistance R_m can be expressed as a linear function of the true resistance R_t and R_m is then given by

$$R_m = g \cdot R_t + R_{off} \tag{1}$$

where R_{off} is an offset and g a gain factor. Gain factor g and the offset R_{off} can be derived from the measurement of the reference resistors, and g is defined by

$$g = \frac{R_{m,50} - R_{m,100}}{R_{t,50} - R_{t,100}} \tag{2}$$

where $R_{t,50}$ and $R_{t,100}$ are the known resistances of the reference resistors. Similarly, the offset R_{off} is defined by

$$R_{off} = R_{m,50} - g \cdot R_{t,50} \tag{3}$$

and the true (corrected) value R_t of the measured resistance is then given by

$$R_t = \frac{R_m - R_{off}}{g} \tag{4}$$

Dropping the subscript t for readability, $R(T)$ has been determined for all TEM sensors according to the above procedure including the correction for offset and gain errors. Data have then been fitted to the Callendar-van Dusen equation using a least squares algorithm. The Callendar-van Dusen equation, which describes the temperature dependence of $R(T)$ for platinum resistance temperature detectors, is given by

$$R(T) = R_0[1 + AT + BT^2 + (T - 100)CT^3] \tag{5}$$

Table 2
Error Sources Taken Into Account for Determining Calibration Uncertainty

Error source	Value (mK)	Distr.	σ (mK)	Remarks
Electronics	1.5	normal	0.3	Data sheet value
Ref. res.	2.0	uniform	1.2	NIST calibration
Ref. thermom.	12.0	uniform	6.9	NIST calibration
Bath stability	7.0	uniform	0.7	Datasheet value
Bath homogeneity	7.0	uniform	4.0	Datasheet value
CvD fitting TEM-P	5.0	uniform	2.9	Including hysteresis
CvD fitting TEM-A	50.0	uniform	28.9	Including hysteresis

Note. Uncertainty, distribution function, and error budget contribution σ are given. Following the relevant standards (VIM, 2004; GUM, 2008), uniformly distributed uncertainties propagate into the total error budget weighted by one over the square root of 3. Data sheet values of stated uncertainties have been verified in the DLR thermal lab. Note that the uncertainty contributions stemming from the electronics and bath stability are reduced by averaging 30 samples during the data reduction process (see text). Stated uncertainties are 1σ confidence limits.

for temperatures below 0 °C and by

$$R(T) = R_0[1 + AT + BT^2]$$

for the range between 0 and 661 °C. Therefore, the result of the calibration is a set of four fitting coefficients R_0, A, B, and C for each sensor. In addition, the misfit of $R(T)$ with respect to the Callendar-van Dusen equation is one contribution to the total calibration error budget (see below).

2.3. Calibration Uncertainty Assessment

Sources of uncertainty for the above calibration procedure are summarized in Table 2 and comprise contributions from the measurement electronics, the calibration uncertainty of the employed reference resistors, the calibration uncertainty of the reference thermometer, the stability of temperatures inside the calibration bath, the homogeneity of temperatures inside the calibration bath, and the misfit between the determined calibration function and the measured resistance values. To propagate these uncertainties to the total calibration uncertainty using Gaussian error propagation, the individual contributions as well as their distribution function need to be known (VIM, 2004; GUM, 2008). While propagation of normally distributed errors is straight forward, uniformly distributed uncertainties need to be weighted by a factor of $1/\sqrt{3}$ (GUM, 2008). In addition, measurement uncertainties for the electronics noise as well as the temperature stability in the calibration bath are reduced by averaging, and the individual contributions to the total error budget are summarized in Table 2.

Given the above contributions, the total temperature uncertainty σ_{abs} is given by

$$\sigma_{abs} = \left(\sigma_{El}^2 + \sigma_{Res}^2 + \sigma_{Therm}^2 + \sigma_{Stab}^2 + \sigma_{Hom}^2 + \sigma_{CvD}^2\right)^{1/2} \quad (6)$$

where σ_{El} is the electrons noise contribution, σ_{Res} the uncertainty contribution for the reference resistors, σ_{Therm} the uncertainty contribution for the reference thermometer, σ_{Stab} the uncertainty associated with temperature fluctuations inside the calibration bath, σ_{Hom} the contribution stemming from temperature inhomogeneities inside the calibration bath, and σ_{CvD} the fitting residual between measured values and the CvD calibration function.

Compared to the total temperature uncertainty, the uncertainty of temperature difference measurements using sensors calibrated using the above setup is slightly reduced, as uncertainties associated with the calibration of reference resistors and thermometers as well as the bath stability are the same for all sensors and thus do not contribute to this error budget. Uncertainty for temperature difference measurements is then given by

$$\sigma_{rel} = \left(\sigma_{El}^2 + \sigma_{Hom}^2 + \sigma_{CvD}^2\right)^{1/2} \quad (7)$$

and uncertainties for the individual sensors will be summarized in the following section.

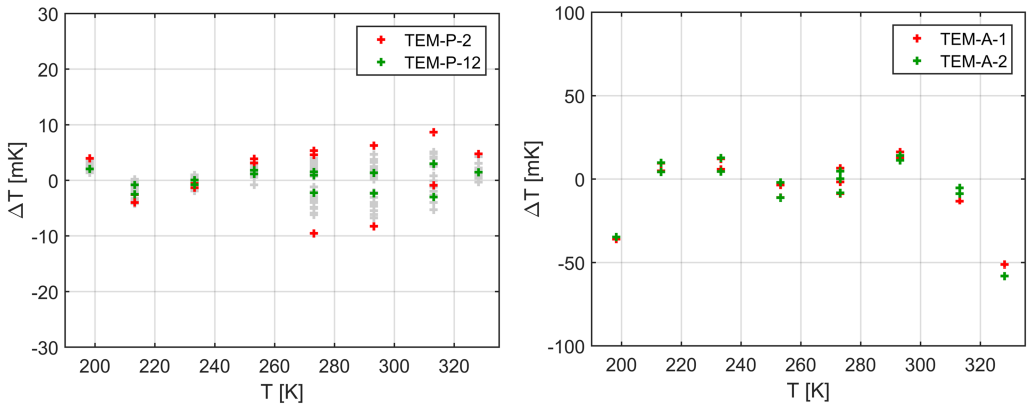

Figure 3. (left) Results of the calibration for the TEM-P sensors showing the fitting residuals with respect to the Callendar-Van Dusen equation as a function of temperature. Sensors showing the smallest and largest deviations are shown in green and red, respectively. (right) Same as on the left, but for the TEM-A sensors.

2.4. Calibration Results

Fitting residuals between the measured $T(R)$ and temperatures calculated using the Callendar-Van Dusen equation are summarized in Figure 3 for all TEM-P and TEM-A sensors in the left and right panels, respectively. In addition, sensors showing the smallest and largest deviations are colored green and red, respectively. Maximum fitting residuals for TEM-P are 10 mK, and sensors show a small hysteresis, particularly above 273.15 K. The cause of the hysteresis is related to the construction of the sensors and strain due to thermal expansion and contraction (Žužek et al., 2010), and this is a known issue with industrial standard PRTs including thin-film, glass-encapsulated, ceramic-encapsulated, and low-hysteresis partially supported sensors (White et al., 2010).

For TEM-A, fitting residuals are much larger than for TEM-P, and misfits of up to 50 mK occur. However, the representation using the Callendar-Van Dusen equation is much better between 220 and 300 K, which is the temperature range relevant for the Martian subsurface. Nevertheless, we will use the full temperature misfit for estimating the calibration uncertainty below.

Calibration results for the individual sensors are summarized in Table 3, where the sensor designation is given along with the CvD fitting coefficients R_0, A, B, and C. In addition, the standard deviation of the fitting residual between the measured temperatures $T(R)$ and temperatures calculated using the Callendar-Van Dusen equation as well as the absolute and relative temperature uncertainty are shown.

TEM-P sensors generally show resistances R_0 between 99.95 and 99.99 Ω at 273.15 K, consistently below the specified 100 Ω for a PT100 sensor. This is a result of the sensor conditioning executed prior to integration (see below). The temperature coefficient of resistance A is 0.0039163 K^{-1} and close to the standard value of 0.00390830 K^{-1} for a PT100 sensor according to the ITS-90 temperature scale (DIN EN 60751, 2009). TEM-A resistance R_0 at 273.15 K is around 375 Ω, as a high resistance is required by the double function of acting as a heating element at the same time as acting as a temperature detector. The coefficient of resistance A for TEM-A is 0.00415 K^{-1}, close to the value of 0.0042 K^{-1} for pure copper.

The 1σ total temperature uncertainty for the TEM-P sensors is 8 to 10 mK, while TEM-A sensor uncertainty is considerably larger and around 30 mK. However, uncertainty of temperature difference measurements using TEM-P are slightly smaller and vary between 4.4 and 6.6 mK. TEM-A is not used for temperature difference measurements, so uncertainties are not given here.

2.5. Sensor Stability

Stability of the TEM sensors is critical for a successful measurement during operations on Mars, and while the above uncertainties apply to sensors directly following calibration, it is important to verify that the obtained calibration functions are still applicable during on-Mars operations. Therefore, a flight-like science tether was exposed to temperature cycles to study the long-term stability of the HP^3 temperature sensors. In total, 1,484 cycles between −90 and +25 °C, 26 cycles between −120 and +75 °C, and 363 cycles between −125 and −10 °C have been performed. Similarly, a flight-like TEM-A was exposed to 257 cycles between −90 and +25 °C and 26 cycles between −120 and +75 °C.

Table 3
Results of the Temperature Calibration of TEM-P and TEM-A Sensors for the HP³ Flight Model

Sensor	R_0 (Ω)	A	B	C	σ_{fit} (mK)	σ_{abs} (mK)	σ_{rel} (mK)
TEM-P-1	99.964	3.9158	−6.68	−3.74	3.5	8.8	5.3
TEM-P-2	99.975	3.9181	−6.73	−3.02	5.3	9.7	6.6
TEM-P-3	99.957	3.9163	−6.65	−3.57	3.8	8.9	5.5
TEM-P-4	99.997	3.9170	−6.65	−3.87	3.1	8.7	5.1
TEM-P-5	99.949	3.9184	−6.66	−3.76	3.7	8.9	5.5
TEM-P-6	99.949	3.9155	−6.66	−3.64	2.4	8.5	4.7
TEM-P-7	99.960	3.9169	−6.64	−3.51	2.5	8.5	4.7
TEM-P-8	99.968	3.9166	−6.61	−3.78	2.9	8.6	4.9
TEM-P-9	99.968	3.9181	−6.66	−3.59	3.1	8.7	5.1
TEM-P-10	99.952	3.9158	−6.61	−3.90	2.0	8.3	4.5
TEM-P-11	99.944	3.9173	−6.60	−4.03	2.3	8.4	4.6
TEM-P-12	99.990	3.9180	−6.60	−4.24	1.9	8.3	4.4
TEM-P-13	99.963	3.9169	−6.58	−4.05	1.9	8.3	4.4
TEM-P-14	99.956	3.9164	−6.60	−4.15	2.0	8.3	4.5
TEM-A-1	378.494	4.15	−0.956	−27.7	28.9	30	N/A
TEM-A-2	373.295	4.15	−0.932	−27.5	28.9	30	N/A

Note. Sensor designation; resistance R_0 at 273.15 K; Callendar-Van Dusen fitting coefficients A, B, and C; standard deviation of the fitting residual σ_{fit}; total absolute temperature uncertainty σ_{abs}; and the total temperature difference uncertainty σ_{rel} between two sensors are given. CvD fitting coefficients A, B, and C (cf. equation (5)) are given in units of 10^{-3} K^{-1}, 10^{-7} K^{-2}, and 10^{-12} K^{-4}, respectively.

Before and after temperature cycling, sensors were calibrated according to the above procedure, and the sensor drift was evaluated by determining the difference between the two sets of CvD calibrations. Results of these calculations are shown in Figure 4 for the TEM-P and TEM-A sensors, where the temperature error induced by thermal cycling is given as a function of temperature. For TEM-P, individual sensors show drift corresponding to up 19 mK, but all sensors tend to drift in a similar direction at most temperatures. On average, sensors show a drift of −15 mK. Concerning temperature differences, large parts of these systematic drifts cancel out, and the distribution of drift induced temperature differences can be fitted by a Gaussian distribution centered on $\mu = 0.3$ mK with a standard deviation of $\sigma = 3.2$ mK. This is shown in the inset in the left-hand panel of Figure 4, for which temperature differences at a target temperature of −55 °C have

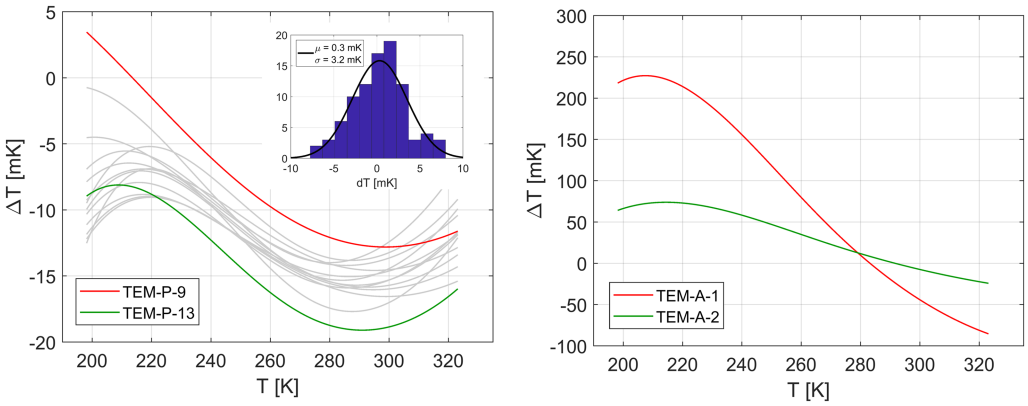

Figure 4. (left) Drift of the TEM-P sensors after thermal cycling showing the temperature difference before and after cycling as a function of temperature. Sensors with the smallest and largest drift are shown in red and green, respectively. The inset shows the distribution of temperature differences between sensors at a target temperature of 220 K including a fit by a Gaussian distribution. (right) Same as left, but for the TEM-A sensors.

been evaluated. Therefore, drift-induced temperature difference errors can be estimated to be 3.2 mK at a 1σ level. However, it is worth noting that HP^3 sensors will only be exposed to a fraction of the number of temperature cycles stated above, such that the error estimate of 3.2 mK must be considered to be a conservative upper bound. Nevertheless, drift error should be taken into account in addition to the uncertainties given in Table 3 when interpreting the data returned from Mars.

Drift of TEM-A sensors under temperature cycles is much larger than that observed for TEM-P and can amount to up to 0.25 K, thus dominating the error budget for the absolute temperature determination. The main part of this error is due to a drift of R_0 (cf. Table 3), and since the determination of thermal conductivity (see below) relies on the measurement of temperature changes at a single sensor only, large parts of the drift cancel out. To first order, temperature changes determined by TEM-A are given by

$$\delta T = \frac{\delta R}{A R_0} \tag{8}$$

where δR is the sensor resistance difference corresponding to the temperature difference δT. The temperature difference uncertainty associated with the uncertainty of R_0 can then be determined from Gaussian error propagation and is given by

$$\Delta(\delta T)^2 = \left(\frac{\partial \delta T}{\partial R_0}\right)^2 \Delta R_0^2 + \left(\frac{\partial \delta T}{\partial A}\right)^2 \Delta A^2 = \left(\frac{\delta R_0}{R_0}\right)^2 \delta T^2 + \left(\frac{\delta A}{A}\right)^2 \delta T^2 \tag{9}$$

Using $\delta R_0 = 0.05\ \Omega$ and $\delta A = 1.5 \cdot 10^{-5}\ \mathrm{K}^{-1}$ as the resistance drift of the sensors and the drift of the temperature coefficient of resistance as measured for the two calibrations, respectively, the uncertainty of temperature difference measurements using the TEM-A sensors is 0.4% and thus negligible in the error budget discussed below.

3. Thermal Conductivity Determination

HP^3 measures thermal conductivity of the regolith k by applying a known amount of heat to the mole's outer hull while simultaneously measuring mole temperature T. While low regolith thermal conductivity will result in a quick rise of mole temperature, large conductivity will yield a slower increase, such that the rate of temperature increase can serve as a measure for k. The method of determining k by applying heat to a thin wire while measuring the self-heating curve is in general known as the LHS method. For the ideal geometry, that is, a thermal probe with large length-to-diameter ratio, heat conduction can be assumed to be one-dimensional in the radial direction only. In this case, the heat conduction equation can be solved analytically subject to the boundary condition of constant heat input along the probe (Carslaw & Jaeger, 1959; Hammerschmidt & Sabuga, 2000b; Jaeger, 1956). For long heating times, the analytical solution can be linearized and thermal conductivity can be approximated by

$$k = \frac{Q}{4\pi}\left(\frac{\partial T}{\partial \ln t}\right)^{-1} \tag{10}$$

where Q is the energy input in units of W m^{-1}, T is probe temperature, and t is time. In order for equation (10) to hold, the dimensionless heating time

$$\tau_{LHS} = \frac{\sqrt{4\kappa t}}{r} \tag{11}$$

needs to be large, where $\kappa = k/\rho c_p$ is regolith thermal diffusivity, ρ is regolith density, c_p is regolith specific heat, and r is the radius of the probe. The error introduced by using the linearization (equation 10) is less than 1% for $\tau_{LHS} \geq 5$ (Hammerschmidt & Sabuga, 2000a). The LHS method and similar approaches have been widely applied, including measurements of thermal conductivity in planetary science applications (Grott et al., 2010; Kömle et al., 2011; Langseth et al., 1972a; Nagihara et al., 2014).

HP^3 measures thermal conductivity using the mole as a modified line-heat source, similar to the approach described above. However, due to the small length to diameter ratio and finite heat capacity, significant deviations from the one dimensional approximation of equation (10) occur. Heat flow from the mole is no longer radial, and inversion of HP^3 data using equation (10) is not possible (Blackwell, 1954; Nagihara et al., 2014).

Rather, for large measurement times, the temperature increase measured at the mole takes the form (Grott et al., 2010; Langseth et al., 1972a)

$$\Delta T(Q,k,S,H,t) = C_1(Q,k,S,H)\ln(t) + C_2(S,H) \tag{12}$$

where S is the ratio of the heat capacities ρc_p of mole and regolith and H the contact conductance between mole and regolith. Note that while C_1 primarily depends on Q and k, some residual dependence on S and H remains, which needs to be taken into account when calculating the thermal conductivity error budget (see below). To first order, thermal conductivity can then be determined from

$$C_1(Q,k,S,H) = \frac{\partial \Delta T(Q,k,S,H,t)}{\partial \ln(t)} \tag{13}$$

We use a numerical thermal model of the HP^3 mole and its environment to determine the temperature increase as a function of time for a given set of model parameters. Fitting of the data is then achieved in a two step process: First, thermal conductivity k is determined by a fit of the numerical model to $\partial \Delta T/\partial \ln(t)$ at times larger than 20 hr (e.g., Grott et al., 2010; Langseth et al., 1972a), corresponding to a dimensionless heating time of $\tau > 6$ under worst case (low conductivity) conditions. Then, the entire curve is fitted by varying S and H.

To validate the numerical model used for fitting equation (13), measurements performed using the HP^3 mole have been compared to results obtained using reference measurements performed using a transient hot strip method (THS; Hammerschmidt & Sabuga, 2000a), which is similar to the LHS method described above. However, a two-dimensional heating strip is used instead of the needle or wire used in the LHS method, as measurements were carried out in granular material with particle diameters in the millimeter range. By using a 6-mm-wide heating strip, thermal contact between probe and regolith simulant could be maximized. Similar to the LHS method, thermal conductivity is determined using the hot strip method by providing a known amount of heat, and thermal conductivity of the material is then given by equation (10) for large heating times

$$\tau_{THS} = \frac{\sqrt{4\kappa t}}{D} \tag{14}$$

Note that in equation (14)D is the width of the strip, while r in equation (11) refers to the radius of the probe. Again, for $\tau_{THS} \geq 5$ the error introduced using equation (10) is less than 1% (Hammerschmidt and Sabuga, 2000b). For typical thermal conductivities expected on Mars close to 0.05 W m^{-1} K^{-1} (Grott et al., 2007) and the geometry of the employed heating strip, heating times t should be larger than 1,400 s.

The THS method has been verified against standard materials spanning the conductivity range between 0.031 and 0.175 W m^{-1} K^{-1}. While this does not fully cover the design range of the HP^3 system (Spohn et al., 2018), which shall measure thermal conductivity down to 0.02 W m^{-1} K^{-1}, the availability of certified standard materials is limited by the thermal conductivity of ambient air, which is close to 0.024 W m^{-1} K^{-1} under standard temperature and pressure conditions. However, being an absolute method of measuring thermal conductivity, there is no intrinsic limit to the applicability range of the THS method, and verification tests have been carried out down to thermal conductivities of 0.0058 W m^{-1} K^{-1} (see below).

3.1. Data Inversion

The self-heating curve of the mole is inverted for regolith thermal conductivity using a simplified thermal model of the mole and tether. The general model setup is illustrated in Figure 5, where the geometry of the model is shown on the left-hand side of the figure. The model consists of four domains, that is, the HP^3 tether (orange), the mole mechanism (light blue), the hull (dark blue), and the TEM-A heaters (red). The mole model is embedded in a fifth domain representing the regolith, and the model is set up in cylindrical symmetry. The computational mesh used in the simulations is shown in the middle of Figure 5 and consists of 5,300 elements. To solve the model, thermophysical properties need to be specified for each domain, and model temperatures are then calculated by solving the heat conduction equation

$$\rho c_p \frac{\partial T}{\partial t} = \nabla(k\nabla T) + q \tag{15}$$

where ρ is density, c_p is specific heat, T is temperature, t is time, k is thermal conductivity, and q is the applied heating power per unit volume. Furthermore, the thermal coupling between the hammering mechanism

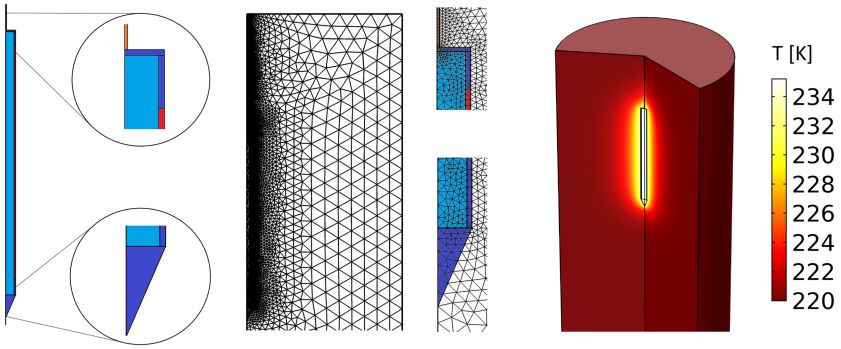

Figure 5. (left) Sketch of the simplified finite element mole model showing the individual domains: hammering mechanism (light blue), outer hull (blue), tether (orange), and TEM-A heater (red). A closeup of the backcap and tip of the mole are also shown. (middle) Computational grid used in the calculations. (right) Example model result assuming a regolith thermal conductivity of 0.05 W m^{-1} K^{-1}, 1 W of heating power, and 24 hr of continuous heating.

and the hull as well as the thermal coupling between hull and regolith need to be prescribed. This is done by defining the contact conductances H_{in} and H, which are given by

$$F_{in} = H_{in}(T_{Mech} - T_{Hull}) \tag{16}$$

and

$$F = H(T_{Hull,Tether} - T_{Reg}) \tag{17}$$

Here, T_{Mech}, $T_{Hull,Tether}$, and T_{Reg} are the temperatures of the mechanism, hull/tether, and regolith, respectively, and F_{in} and F are the heat fluxes across the different interfaces.

Geometrical and material parameters used in the finite element model are summarized in Table 4. The mole has a diameter of 2.7 cm, a length of 39.3 cm, and a total mass of 850 g. The major part of the mass is distributed in the mole hull including tip and backcap, while 40% of the mass are taken up by the mechanism. Heat transport inside the mole is modeled by conduction only, and imperfect coupling between the inner and out parts of the mole is modeled assuming a finite contact conductance. Bulk thermal properties of the mole hull and mechanism are mass averages of the respective mole materials. Due to numerical difficulties associated with the modeling of thin layers, the HP^3 tether is modeled as a roundwire cable with a thermal conductance equivalent to the flight hardware. Tether contact conductance to the regolith is given by equation (17).

To fully define the model, thermophysical parameters for the regolith also need to be prescribed. We assume a heat capacity of 670 J kg^{-1} K^{-1} and a density of 1,450 kg m^{-3} (Morgan et al., 2018), while regolith thermal conductivity is a free fitting parameter. Given an initially homogeneous temperature distribution and prescribing the heating power Q for the TEM-A heaters, the model is time integrated for the prescribed heating period, which is generally chosen to be 24 hr. Model output is then compared to the test data, and regolith thermal conductivity is varied until the best fitting temperature increase $\partial \Delta T / \partial \ln(t)$ is obtained. Keeping regolith thermal conductivity and heat capacity fixed, the entire curve is then fitted by varying regolith density and outer boundary contact conductance H.

3.2. Test Setup

The capability of determining thermal conductivity over the required range using the HP^3 mole as a modified LHS has been verified in thermal vacuum tests. In the tests, two identical test cylinders have been filled with PMMA (Polymethyl methacrylate, also known as acrylic glass) granulate, and the HP^3 mole as well as a transient hot strip have been inserted into the respective containers. Cylinders were then placed inside a vacuum chamber, and the general setup of the test is shown in Figure 6. During the tests, HP^3 TEM-A sensors inside the mole were controlled using a flight equivalent HP^3 backend electronics, while the THS was controlled using bench electronics. While the PMMA bulk material has a thermal conductivity close to 0.2 W m^{-1} K^{-1}, the granulate has a thermal conductivity of 0.1 W m^{-1} K^{-1} at standard pressure and temperature, as has been determined using the THS measurement setup. This is further reduced at lower pressures (see, e.g., Hütter et al., 2008).

Table 4
Parameters Used to Define the Simplified Mole Model for Thermal Conductivity Inversion

Parameter	Value	Units	Description
R_{Tether}	0.001	m	Modeled width of the tether
R_{Mole}	0.0135	m	Radius of the mole
D_{Wall}	0.002	m	Wall thickness of the mole hull
L_{Tip}	0.031	m	Length of the mole tip
L_{Up}	0.018	m	Length of the upper part of the hull
L_{Heater}	0.321	m	Length of the TEM-A heater
L_{Down}	0.021	m	Length of the lower part of the hull
k_{Hull}	23	W m^{-1} K^{-1}	Thermal cond. of the hull
k_{Mech}	67	W m^{-1} K^{-1}	Thermal cond. of the mechanism
k_{Tether}	38.2	W m^{-1} K^{-1}	Thermal cond. of the Tether
$c_{p,Hull}$	510	J kg^{-1} K^{-1}	Heat capacity of the Hull
$c_{p,Mech}$	340	J kg^{-1} K^{-1}	Heat capacity of the mechanism
$c_{p,Tether}$	1050	J kg^{-1} K^{-1}	Heat capacity of the tether
m_{Mech}	0.654	kg	Mass of the mechanism
m_{Hull}	0.188	kg	Mass of the hull
ρ_{Tether}	1420	kg m^{-3}	Density of the tether
H_{in}	150	W m^{-2} K^{-1}	Inner boundary contact conductance
H	250	W m^{-2} K^{-1}	Outer boundary contact conductance

After an initial characterization of the test setup at ambient pressure, the vacuum chamber was first fully evacuated and then refilled with 50 mbar of Argon. It was then stepwise pumped down to 8 mbar and high-vacuum conditions. At each step, pressure was monitored until it stabilized and power was supplied to the TEM-A heating foils for 24 hr, identical to the heating times foreseen during on Mars operations. Note, however, that due to the limited size of the test cylinders, only the first 150 min of temperature data was used in the inversion. This eliminates boundary effects, which for the size of the containers start to be important at $t > 300$ min. For the THS measurement, a heating time of 1 hr was chosen in accordance with equation (14). After completion of the heating experiments, heat was allowed to dissipate for 48 hr before repeating the experiments at the next pressure step.

Results of the verification tests for the THS reference measurement and the HP^3 TEM-A measurement at 8 mbar are shown in Figure 7. The left-hand side of Figure 7 shows the THS result, where thermal conductivity

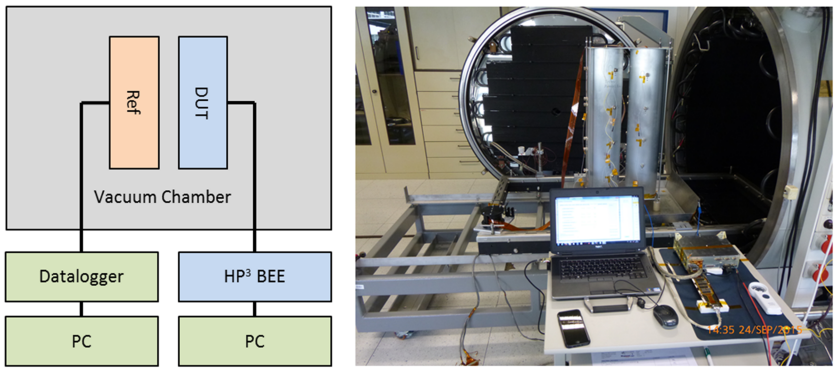

Figure 6. (left) Schematics of the setup for thermal conductivity tests. The device under test, that is, the mole including the TEM-A sensors, is placed inside the right cylinder, while the transient hot strip (THS) reference measurement is placed inside the left cylinder. Both cylinders are moved into the vacuum chamber. Data for the reference measurement are logged by benchtop electronics, while the TEM-A data are taken by the HP^3 electronics. (right) Picture of the setup in the DLR Space Simulation Chamber with the cylinders still outside the chamber.

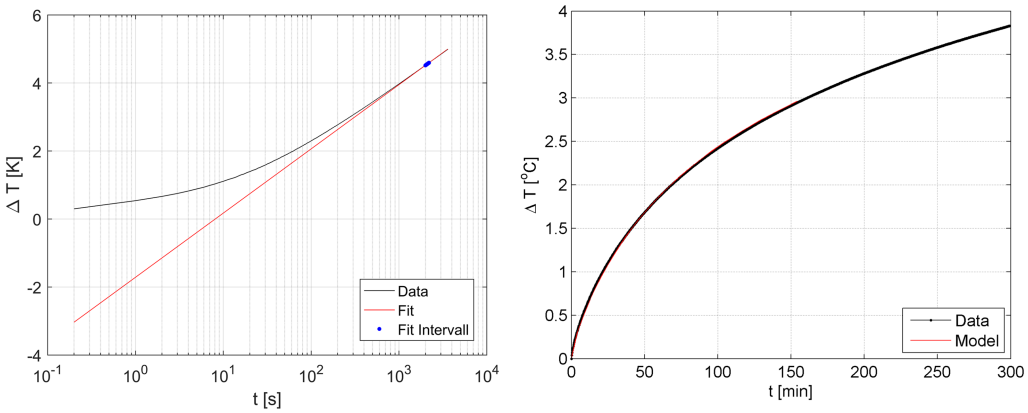

Figure 7. Results for the TEM-A test at 8 mbar. (left) Temperature as a function of time for the THS reference measurement. Data (black) as well as best asymptotic fit (red) are shown along with the fitting interval (blue). (right) Temperature as a function of time for the TEM-A measurement. Data (black) as well as best fit (red) are shown.

was determined from the slope of the logarithmic temperature increase at the fitting interval indicated in blue. Data were fitted between 2,000 and 2,200 s, corresponding to $\tau_{THS} = 5$, and a thermal conductivity of 0.075 W m^{-2} K^{-1} was obtained. Results of the TEM-A measurement are shown on the right-hand side of the figure, where temperature is given as a function of time. Data were fitted using a least squares algorithm and the HP^3 TEM-A thermal model described in section 3.1, and a thermal conductivity of 0.072 W m^{-2} K^{-1} was obtained. While measurements under high-vacuum conditions and 50 mbar (not shown) differ from the results obtained using the reference measurements by less than 1%, the measurement at 8 mbar is slightly less accurate. This is likely due to residual background temperature drift, which was not actively controlled in the present experiments. Results and parameters used in the fitting are summarized in Table 5, and in summary the model used for fitting TEM-A data was found to be accurate to within 4% over the full range of thermal conductivities expected on Mars. It is worth noting that for measurements on Mars background temperature drift before starting a TEM-A measurement will be monitored at the location of the mole, such that potential drift can be corrected for.

3.3. Thermal Conductivity Error Budget

Contributions to the thermal conductivity error budget stem from measurement errors connected to temperature drift of the sensors σ_{Temp} as well as uncertainties associated with determining the heat input into the TEM-A foils σ_Q. Furthermore, the dependence of $C_1(Q, k, S, H)$ (cf. equation (13)) on the ratio of heat capacities S and the contact conductance H introduce uncertainties σ_S and σ_H. Finally, the model error σ_{mod} and the uncertainty of the reference measurement itself σ_{THS} need to be taken into account. Taken together, the total thermal conductivity uncertainty is given by

$$\sigma_k = \left(\sigma_{Temp}^2 + \sigma_Q^2 + \sigma_S^2 + \sigma_H^2 + \sigma_{mod}^2 + \sigma_{THS}^2\right)^{1/2} \tag{18}$$

Table 5
Results of the TEM-A Tests Under Varying Pressure Conditions

p (mbar)	k_{THS} (W m^{-1} K^{-1})	k_{TEM-A} (W m^{-1} K^{-1})	Δk (%)
$4.5{\cdot}10^{-6}$	0.0058	0.0058	< 1[a]
8	0.075	0.072	4
50	0.084	0.084	< 1

Note. Pressure in the chamber p, thermal conductivity determined by the THS reference measurement k_{THS}, thermal conductivity determined by TEM-A k_{TEM-A}, and the deviation of TEM-A results from the reference measurement Δk are given.
[a]Note that in order to fit the high-vacuum data, contact conductances $H = 4$ W m^{-2} K^{-1} and $H_{in} = 6$ W m^{-2} K^{-1} have been assumed. This is consistent with conductances derived from Apollo thermal conductivity measurements under vacuum conditions (Grott et al., 2010; Langseth et al., 1972a).

Table 6
Error Sources Taken Into Account for Determining the Thermal Conductivity Uncertainty Budget

Error source	Value (%)	Distr.	σ (%)	Remarks
Temperature drift	0.4	normal	0.4	Calibration
Heat input	0.1	normal	0.1	Test
Regolith parameter	1.5	uniform	0.9	Analysis
Thermal contact	2	uniform	1.2	Analysis
Modeling	4	uniform	2.3	Analysis
Reference method	2.5	normal	2.5	Method uncert.
Total 1σ uncertainty			3.7	

Note. Uncertainty, distribution function, and error contribution σ are given. Following the relevant standards (GUM, 2008; VIM, 2004), uniformly distributed uncertainties propagate into the total error budget weighted by one over the square root of 3. Stated uncertainties are 1σ confidence limits.

As discussed in section 2.5, $\sigma_{Temp} \approx 0.4\%$, while the heat input uncertainty is $\sigma_Q \approx 0.1\%$ (Spohn et al., 2018). σ_S has been determined by systematically varying regolith density in the model while fitting the slope of the temperature increase $\partial \Delta T / \partial \ln(t)$ and keeping all other parameters constant (cf. equation (13)). As a result, σ_S was found to be 1.5% when varying regolith density by a factor of 2. Similarly, σ_H was determined by varying H between 250 and 25 W m^{-2} K^{-1}, and $\sigma_H = 2\%$ was determined. Modeling uncertainty σ_{mod} is estimated to be $< 4\%$ as determined during verification testing (see above). As the density and heat capacity of the mole are known by construction and the heat capacity of the martian regolith is known with only minor uncertainties (Morgan et al., 2018; Vu et al., 2019), these parameters do not significantly contribute to the total measurement uncertainty.

To be able to trace the results obtained using the TEM-A sensor system to national standards, the 1σ uncertainty of the THS reference measurement also needs to be taken into account. Uncertainty of the method is estimated to be 2.5% (Hammerschmidt and Sabuga, 2000a), and uncertainty contributions to the total thermal conductivity error budget are summarized in Table 6. The total 1σ thermal conductivity uncertainty was found to be 3.7%, slightly larger than the uncertainty estimate of 2.5% given in Spohn et al. (2018), which did not include modeling errors and uncertainty caused by sensor drift. However, the difference to the estimate given here is small and instrument performance is well within measurement requirements.

The thermal conductivity error budget is dominated by contributions stemming from the uncertainties associated with the numerical model, although the observed maximum deviation between model and reference method is likely a conservative upper limit. Furthermore, the total uncertainty cannot be smaller than 2.5%, the intrinsic uncertainty of the THS method. At large heating times, uncertainties associated with the unknown regolith properties S and thermal contact conductance H are of secondary importance, and uncertainties introduced by sensor drift and electrical measurements are generally negligible.

4. Tiltmeter Calibration

4.1. Tilt Determination

HP^3 uses two 2-axis ADXL203 static tiltmeters to determine the attitude of the mole with respect to the local gravity vector. The tiltmeters are mounted inside the HP^3 mole's payload compartment and they are mechanically decoupled from the shock environment inside the mole by a set of dampening springs. Accelerometers are read out by 24-bit analogue-to-digital converters inside the HP^3 backend electronics, which is located inside the InSight lander's warm electronics box. STATIL signals are transmitted through the science and engineering tethers, which connect the mole to the HP^3 support structure and the support structure to the lander, respectively. An overview of the HP^3 system design is given in Spohn et al. (2018).

The STATIL sensor assembly is shown in the left-hand panel of Figure 8, where sensors are mounted on the STATIL flexprint PCBs (green). PCBs themselves are mounted at an angle with respect to the mole axis (vertical in the picture), and the shock dampening system (gray) is integrated into the HP^3 mole payload cage (blue). In the following, the axes of the upper tiltmeter will be referred to as X and Y, while the axes of the bottom tiltmeter will be denoted A and B.

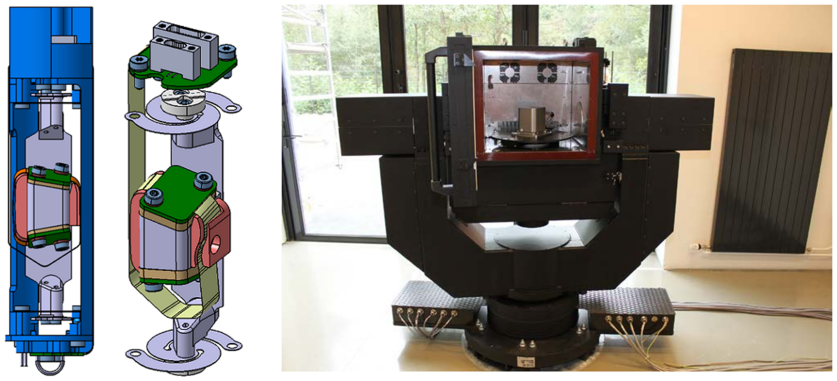

Figure 8. (left) Two 2-axis STATIL sensors mounted on printed circuit boards (PCB) (green) integrated in their dampening fixture (gray) inside the mole payload cage (blue). (middle) Same as left, but without the mole payload cage and showing three PCBs. S-shaped dampening springs are located at the top and bottom of the assembly. STATIL sensors are mounted on the bottom and middle PCB and are inclined with respect to the mole axis (vertical in the image). The upper accelerometer axes are denoted X and Y, while the bottom accelerometer axes are denoted A and B. (right) Acutronic AC3347 rotation table equipped with a climate chamber used for STATIL calibration.

The measured STATIL output voltage V follows a sinusoidal dependence on the angle ϕ with respect to local gravity. However, before processing STATIL readings and converting them into angles, electrical offsets generated inside the backend electronics need to be accounted for. These are caused by line resistances in the tethers and other electronics offsets. Furthermore, a shared ground line of STATIL with the tether length monitoring (TLM) system results in a voltage offset whenever STATIL and TLM are operated in parallel. The first of these offsets is denoted V_0 and results in a shift of the zero crossing of the sine, while the second offset is denoted V_{TLM}. In addition, mounting uncertainties of the tiltmeters with respect to the mole axis need to be considered, and a corresponding correction V_{align} needs to be applied. In summary, corrected STATIL readings are given by

$$V_c(\phi) = V(\phi) + V_{align} \cdot g + V_0 \cdot g - V_{TLM} \cdot c \tag{19}$$

where $g = 0.3784$ accounts for the reduced martian gravity and $c = 1$ if TLM is switched off and 0 otherwise. The conversion between measured (corrected) signal $V_c(\phi)$ and angle ϕ with respect to gravity is then given by

$$\phi = \arcsin\left(\frac{V_c(\phi)}{V_{amp} \cdot g}\right) \tag{20}$$

where the amplitude $V_{amp} = (V_{max} - V_{min})/2$ is determined during ground calibration for each axis of the tiltmeters and V_{min} and V_{max} represent the maximum and minimum output when rotating the sensors through 360°.

As the two accelerometers are redundant, two different realizations of the local gravity vector can be calculated. Given STATIL angles ϕ_X, ϕ_Y, ϕ_A, and ϕ_B with respect to local gravity, gravity vectors can be reconstructed by

$$\vec{g}_{X,Y} = \begin{pmatrix} \sin(\phi_X) \\ \sin(\phi_Y) \\ \sqrt{1 - \sin^2(\phi_X) - \sin^2(\phi_Y)} \end{pmatrix} \tag{21}$$

and

$$\vec{g}_{A,B} = \begin{pmatrix} \sin(\phi_A) \\ \sin(\phi_B) \\ \sqrt{1 - \sin^2(\phi_A) - \sin^2(\phi_B)} \end{pmatrix} \tag{22}$$

in the STATIL X/Y and A/B coordinate frames, respectively.

Table 7
Euler Rotation Angles α, β, and γ for the Transformation Between the STATIL Coordinate Frames and the HP³ Mole's Coordinate Frame for the X/Y and A/B Axis Pairs

Axis system	α (°)	β (°)	γ (°)
X/Y	225	14	−80
A/B	225	−14	−55

The direction of the gravity vector in the HP³-mole frame can then be obtained by a coordinate transformation using Euler Angles. Adopting the y-convention (also known as the z-y'-z'' convention) and denoting rotations by α, β, and γ, the gravity vectors in the mole coordinate system are obtained by the inverse Euler transformations

$$\vec{g}_{X,Y,Mole} = \mathbf{M}^{T}_{\alpha\beta\gamma}\vec{g}_{X,Y} \tag{23}$$

and

$$\vec{g}_{A,B,Mole} = \mathbf{M}^{T}_{\alpha\beta\gamma}\vec{g}_{A,B} \tag{24}$$

respectively. Angles α, β, and γ to be employed in this transformation are given in Table 7.

4.2. Calibration Setup and Procedure

STATIL tilt sensors have been calibrated after integration onto their PCBs using an Acutronic AC3347 rotation table. The rotation table has a positioning uncertainty of better than 0.001°, and orthogonality of the axes is better than 0.001°. Positioning resolution is 0.00001°, and a climate chamber can be integrated into the setup to characterize sensors at temperatures between −50 and +80 °C. The rotation table and climate chamber are shown in the right-hand panel of Figure 8.

For the calibration, STATIL flexprints were fixed on an adapter plate and mounted inside the climate chamber as part of the rotation table assembly. Electrical signals were recorded by a flight equivalent HP³ backend electronics (Spohn et al., 2018), which was also mounted inside the chamber. Calibration was then carried out at temperatures of +23 and −40 °C, and the assembly was rotated through 360° to identify the maximum and minimum readings for all four axes. Results of the calibration are summarized in Table 8, where the average values between the room temperature and cold calibration runs are given. Reported values are the average maximum signal $V_{\max}$, the average minimum signal $V_{\min}$, as well as the maximum variation $|\Delta V|$ between warm and cold calibration results. The latter was used to estimate temperature drift of the sensors as part of the total angle uncertainty budget (see Sec. 4.3).

The zero-g bias voltage V_0 of the tilt sensors was determined during an HP³ cruise checkout. During cruise, STATIL angles should read 0, as tiltmeters should be in their unloaded positions. Therefore, any offsets from 0 observed during zero-g conditions must be either manufacturing tolerances or electronics offsets. The zero-g bias voltage V_0 is given in Table 8 and corresponds to the average STATIL readings during cruise. Note that during the checkout, TLM was operated in parallel to STATIL.

To determine the alignment of tilt sensors inside the mole, the procedure of rotating sensors through 360° was repeated after integration of the STATIL assembly into the HP³ mole (Spohn et al., 2018). However, due to size limitations inside the climate chamber, these measurements were performed at room temperature

Table 8
Results of the STATIL Sensor Calibrations for the Four STATIL Axes X, Y, A, and B

	X	Y	A	B
$V_{\max}$ [DN]	2,961,148	2,771,689	2,927,286	2,989,777
$V_{\min}$ [DN]	−2,957,630	−2,993,840	−2,975,555	−2,897,468
$\|\Delta V\|$ [DN]	73,679	99,434	93,698	−54,072
V_{align} [DN]	−1,702	−20,270	9,421	7,909
V_0 [DN]	5,672	−28,461	43,371	−14,958
V_{TLM} [DN]	15,822	13,419	18,105	12,012

Note. Maximum $V_{\max}$ and minimum $V_{\min}$ sensor signals when rotating the sensors through 360° were determined during ground calibration, and average values between the calibration runs at +23 and −40 °C are reported along with the maximum variation $|\Delta V|$ between warm and cold calibration results. The tilt offset V_0 was determined during cruise under zero-g conditions. The alignment offset V_{align} and the electrical offset V_{TLM} caused by the tether length monioring system (TLM) are also given.

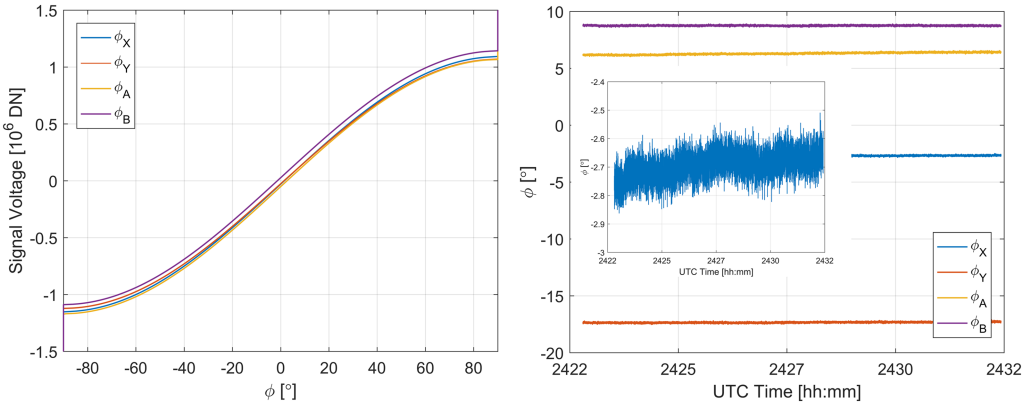

Figure 9. (left) Raw signal voltage as a function of angle with respect to local gravity for the four STATIL axes. (right) Angles of the four STATIL axes as a function of time during the first on Mars tilt measurement. During the measurement, the HP^3 mole was inside the support structure, which was mounted on the lander deck. The inset shows a closeup of the angle readings on the X axis. Electrical noise of the measurement is 0.05°.

only. For the measurements, the HP^3 flight mole was placed inside a mounting fixture, which was then attached to the baseplate of the rotation table, and the differences between values expected for the nominal alignment and the actual alignment were measured. The resulting offsets are tabulated in Tab. 8.

Finally, the electrical offset V_{TLM} introduced by operating the TLM in parallel with STATIL were determined using flight data during Mars surface operations. This has the advantage that the complete measurement chain in flight configuration could be used. To determine the offset, a 10-min tilt measurement including TLM operation was performed, followed by a 20-min tilt measurement with TLM switched off. Again, resulting offsets are given in Table 8.

Results of the calibration are illustrated in Figure 9, where signal voltage is shown as a function of angle for the four STATIL axes on the left-hand side of the figure. On the right-hand side, STATIL angles as measured after landing are shown as a function of time. These largely reflect the inclined mounting of the tiltmeters with respect to vertical, and the attitude of the HP^3 mole can be derived from ϕ_X, ϕ_Y, ϕ_A, and ϕ_B using equation (21)–(24). As a result, a total inclination of the HP^3 mole with respect to gravity of 3.92° and 3.98° is obtained using the X/Y and A/B axis pairs, respectively. The inset on the right-hand side of the figure shows a closeup of ϕ_A as a function of time, indicating measurement noise corresponding to 0.05°.

4.3. Error Budget

To be negligible in the overall heat flow error budget, the attitude of the HP^3 mole with respects to the local gravity vector has to known to within ±3°. Contributions to the overall uncertainty budget consist of the alignment uncertainty σ_{Align}, the temperature drift σ^2_{Temp}, as well as electronics noise σ_{El}. Given these uncertainties, the total tilt uncertainty σ_{tilt} can be calculated by Gaussian error propagation and is given by

$$\sigma_{tilt} = \left(\sigma^2_{Align} + \sigma^2_{Temp} + \sigma^2_{El}\right)^{1/2} \tag{25}$$

While the rotation of sensors through 360° during initial calibration ensures an accurate characterization of sensor output, uncertainty remains with respect to the alignment of sensors inside the mole. While absolute uncertainty of the tilt determined by the rotation table is better than 0.001°, total alignment uncertainty is ultimately limited by manufacturing tolerances of the mounting fixtures used during the test. These are estimated to amount to 0.1°, representing a moderate contribution to the total uncertainty budget.

Temperature drift of the tilt sensors has been estimated from the initial calibration at +23 and −40 °C. While the calibration coefficients reported in Table 8 represent average values, the spread observed over the operating temperature range has been used to estimate maximum temperature drift. Deviations $|\Delta V|$ have been used to estimate tilt uncertainty using equation (20), and temperature drift was found to be the major contribution to the uncertainty budget.

Electronics noise limits the resolution of the tilt measurements, and the noise contribution to the total uncertainty budget was determined from tilt data obtained during the post landing HP^3 checkout performed on

Table 9
Error Sources Taken Into Account for Determining Angle Calibration Uncertainty

Error source	Value (°)	Distr.	σ (°)	Remarks
Alignment	0.1	uniform	0.06	Manufact. tolerances
Temperature drift	0.35	uniform	0.2	Calibration
Electronics noise	0.05	normal	0.05	Flight data
Total 1σ uncertainty			0.22	

Note. Uncertainty, distribution function, and error budget contribution σ are given. Following the relevant standards (GUM, 2008; VIM, 2004), uniformly distributed uncertainties propagate into the total error budget weighted by one over the square root of 3. Stated uncertainties are 1σ confidence limits.

Mars. Electronics noise is a small contribution to the total error budget, and the STATIL subsystem is capable of resolving tilt differences of 0.05° at a 1σ level.

All uncertainty contributions are summarized in Table 9 and the overall tilt uncertainty is 0.22° at a 1σ level. As is evident from the table, temperature drift of the sensors is the dominating factor in the error budget, and the overall performance of the tilt sensors satisfies the measurement requirement (Spohn et al., 2018) of ±3° by a huge margin.

5. Summary and Conclusions

The HP^3 on the InSight Mars mission will determine the Martian planetary heat flow by measuring the subsurface thermal gradient and thermal conductivity to a depth of 5 m. Subsurface temperatures will be measured using industry standard (PT100) platinum resistance thermometers, which can be calibrated to the 10-mK level (Yamazawa et al., 2011). HP^3 will determine the depth of sensors in the ground from mole tilt and tether length measurements, and regolith thermal conductivity will be determined using the HP^3 mole as a modified LHS (Spohn et al., 2018).

HP^3 PT100 temperature sensors have been tested under relevant environmental conditions and were found to be extremely stable with respect to mechanical and thermal stress. Sensors have been calibrated in the range between −75 and +55 °C by comparison with a secondary standard reference thermometer. At a 1σ level, the total temperature uncertainty was found to be better than 10 mK, while the temperature difference uncertainty was found to be better than 5 mK. This compares well with the uncertainties estimated for the temperature sensors on the Apollo heat flow probes, for which absolute and relative measurement uncertainties of 50 and 1 mK are estimated in the ±2 K measurement range, respectively (Arthur D. Little, inc., 1969; Langseth et al., 1972b, 1973). For reference, the temperature uncertainty of the thermocouples embedded in the Apollo heat flow probe's harness has temperature uncertainties of 0.5 K. For HP^3, potential absolute post calibration sensor drift was found to be below 15 mK, while relative drift of the sensors is below 3.2 mK.

HP^3 TEM-A heating foils are simultaneously used as temperature sensing elements, and their resistance as a function of temperature has been calibrated by a comparison calibration using the same setup described above. Their calibration range also covers −75 and +55 °C and absolute temperature uncertainty of the heaters/sensors was found to be 30 mK at a 1σ level at the time of calibration. While sensors do drift by up to 0.25 K under thermal stress, temperature uncertainty is a minor contribution to the total thermal conductivity uncertainty budget.

We use a simplified thermal model of the HP^3 mole and tether to determine thermal conductivity from the mole's self-heating curve, an approach similar to that used for the inversion of the Apollo thermal conductivity data (Grott et al., 2010; Langseth et al., 1972a). The thermal conductivity uncertainty budget is dominated by the principal uncertainty of the LHS method itself, but unknown regolith density and modeling uncertainties also play a role. Overall, the current approach allows for a determination of thermal conductivity with an uncertainty of 3.7% at a 1σ level, which compares favorably with the thermal conductivity uncertainty of 10% estimated for the Apollo heat flow probes (Langseth et al., 1972a).

To reconstruct the HP^3 mole path and determine the depth of the individual PT100 sensors, the attitude of the mole during penetration is measured using tiltmeters. These have been calibrated on ground using a

high-precision rotation table, while electrical and zero-g offsets have been determined during ground testing and cruise. Furthermore, temperature drift of the sensors has been estimated. In total, angle uncertainty was found to be better than 0.22° at a 1σ level.

Acknowledgments
All calibration data necessary for the interpretation of HP^3 raw data are available in the tables presented. Raw calibration data and a COMSOL finite element model of the HP^3-mole are available online (https://doi.org/10.6084/m9.figshare.c.4593926.v2). The design, building of, and research into the HP^3 have been supported by the German Aerospace Center DLR, by NASA, the ÖAW, and the Polish Academy of Science. This paper is InSight Contribution 94.

References

Arthur D. Little, inc. (1969). Lunar heat flow probes for the ALSEP heat flow experiment.

Banerdt, W. B., Banerdt, W. B., Smre-kar, S., Alkalai, L., Hoffman, T., Warwick, R., et al. (2012). Insight: An integrated exploration of the interior of Mars. In *Proceedings of the 43rd Lunar and Planetary Science Conference* (p. 2838). Texas: The Woodlands.

Blackwell, J. H. (1954). A transient flow method for determination of thermal constants of insulating materials in bulk. *Journal of Applied Physics*, *25*, 137–144.

Carslaw, H. S., & Jaeger, J. C. (1959). *Conduction of heat in solids* (2nd ed.). Oxford, UK: Clarendon.

Davies, J. H. (2013). Global map of solid Earth surface heat flow. *Geochemistry, Geophysics, Geosystems*, *14*, 4608–4622. https://doi.org/10.1002/ggge.20271

Davies, J. H., & Davies, D. R. (2010). Earth's surface heat flux. *Solid Earth*, *1*, 5–24.

DIN EN 60751 (2009). Industrial platinum resistance thermometers and platinum temperature sensors, German Institute for Standardisation.

Golombek, M., Kipp, D., Warner, N., Daubar, I. J., Fergason, R., Kirk, R. L., et al. (2017). Selection of the InSight landing site. *Space Science Reviews*, *211*(1-4), 5–95. https://doi.org/10.1007/s11214-016-0321-9

Grott, M., Baratoux, D., Hauber, E., Sautter, V., Mustard, J., Gasnault, O., et al. (2013). Long-term evolution of the Martian crust-mantle system. *Space Science Reviews*, *172*(1), 49–111. https://doi.org/10.1007/s11214-012-9948-3

Grott, M., Helbert, J., & Nadalini, R. (2007). Thermal structure of Martian soil and the measurability of the planetary heat flow. *Journal of Geophysical Research*, *112*, E09004. https://doi.org/10.1029/2007JE002905

Grott, M., Knollenberg, J., & Krause, C. (2010). Apollo lunar heat flow experiment revisited: A critical reassessment of the in situ thermal conductivity determination. *Journal of Geophysical Research*, *115*, E11005. https://doi.org/10.1029/2010JE003612

GUM (2008). Evaluation of measurement data—Guide to the expression of uncertainty in measurement, Joint Committee for Guides in Metrology, JCGM 100:2008.

Hammerschmidt, U., & Sabuga, W. (2000a). Transient Hot Strip (THS) method: Uncertainty assessment. *International Journal of Thermophysics*, *21*(1), 217–248.

Hammerschmidt, U., & Sabuga, W. (2000b). Transient hot wire (THW) method: Uncertainty assessment. *International Journal of Thermophysics*, *21*(6), 1225–1278.

Hütter, E. S., Kömle, N. I., Kargl, G., & Kaufmann, E. (2008). Determination of the effective thermal conductivity of granular materials under varying pressure conditions. *Journal of Geophysical Research*, *113*, E12004. https://doi.org/10.1029/2008JE003085

Jaeger, J. C. (1956). Conduction of heat in an infinite region bounded internally by a circular cylinder of a perfect conductor. *The Australian Journal of Physiotherapy*, *9*(2), 167–179. https://doi.org/10.1071/PH560167

Jaupart, C., & Mareschal, J. C. (2015). Temperatures, heat, and energy in the mantle of the Earth. *Treatise on Geophysics*, *6*, 217. https://doi.org/10.1016/B978-0-444-53802-4.00114-7

Kömle, N. I., Hütter, E. S., Macher, W., Kaufmann, E., Kargl, G., Knollenberg, J., et al. (2011). In situ methods for measuring thermal properties and heat flux on planetary bodies. *Planetary and Space Science*, *59*(8), 639–660. https://doi.org/10.1016/j.pss.2011.03.004

Langseth, M. B., & Keihm, S. J. (1977). In-situ measurements of lunar heat flow, in: NASA, Washington The Soviet-Am. Conf. on Cosmochem. of the Moon and Planets, 283-293, SEE N78-12925 03-90.

Langseth, M. G., Clark, S. P., Chute, J. L., Keihm, S. J., & Wechsler, A. E. (1972a). The Apollo 15 lunar heat-flow measurement. *Earth, Moon, and Planets*, *4*(3-4), 390–410. https://doi.org/10.1007/BF00562006

Langseth, M. G., Clark, S. P., Chute, J. L., Keihm, S. J., & Wechsler, A. E. (1972b). Heat flow experiment, in Apollo 15: Preliminary Science Report, Rep. SP-289, pp. 1-23, chap. 11, Natl. Aeronaut. and Space Admin., Washington, D.C..

Langseth, M. G., Keihm, S. J., Chute, J. L. (1973). Heat flow experiment, in Apollo 17: Preliminary Science Report, Rep. SP-330, pp. 1-24, chap. 9, Natl. Aeronaut. and Space Admin., Washington, D. C..

Langseth, M. G., Keihm, S. J., & Peters, K. (1976). Revised lunar heatflow values. *Proceedings of the Seventh Lunar Science Conference 7th*, *7*, 3143–3171.

Morgan, P., Grott, M., Golombek, M., Delage, P., Lognonné, P., Piqueux, S., et al. (2018). A pre-landing assessment of regolith properties at the InSight landing site. *Space Science Reviews*, *214*(6), 104.

Nagihara, S., Hedlund, M., Zacny, K., & Taylor, P. T. (2014). Improved data reduction algorithm for the needle probe method applied to in-situ thermal conductivity measurements of lunar and planetary regoliths. *Planetary and Space Science*, *92*, 49–56. https://doi.org/10.1016/j.pss.2013.12.012

Parro, L. M., Jiménez-Díaz, A., Mansilla, F., & Ruiz, J. (2017). Present-day heat flow model of Mars. *Scientific Reports*, *7*, 45629. https://doi.org/10.1038/srep45629

Plesa, A.-C., Padovan, S., Tosi, N., Breuer, D., Grott, M., Wieczorek, M. A., et al. (2018). The thermal state and interior structure of Mars. *Geophysical Research Letters*, *45*, 12,198–12,209. https://doi.org/10.1029/2018GL080728

Plesa, A.-C., Tosi, N., Grott, M., & Breuer, D. (2015). Thermal evolution and Urey ratio of Mars. *Journal of Geophysical Research: Planets*, *120*, 995–1010. https://doi.org/10.1002/2014JE004748

Pollack, H. N., Hurter, S. J., & Johnson, J. R. (1993). Heatflow from the Earth's interior-Analysis of the global data set. *Reviews of Geophysics*, *31*, 267–280. https://doi.org/10.1029/93RG01249

Ruiz, J. (2014). The early heat loss evolution of Mars and their implications for internal and environmental history. *Scientific Reports*, *4*, 4338. https://doi.org/10.1038/srep04338

Smrekar, S. E., Lognonné, P., Spohn, T., Banerdt, W. B., Breuer, D., Christensen, U., et al. (2019). Pre-mission InSights on the Interior of Mars. *Space Science Reviews*, *215*, 3. https://doi.org/10.1007/s11214-018-0563-9

Spohn, T., Grott, M., Smrekar, S. E., Knollenberg, J., Hudson, T. L., Krause, C., et al. (2018). The heat flow and physical properties package (HP^3) for the InSight mission. *Space Science Reviews*, *214*(96). https://doi.org/10.1007/s11214-018-0531-4

VIM (2004). International vocabulary of basic and general terms in metrology, ISO VIM DGUIDE 99999, International Organization for Standardization.

Vu, T. H., Piqueux, S., Choukroun, M., Edwards, C. S., Christensen, P. R., & Glotch, T. D. (2019). Low-temperature specific heat capacity measurements and application to Mars thermal modeling. *Icarus*, *321*, 824–840. https://doi.org/10.1016/j.icarus.2018.10.004

Warren, P. H., & Rasmussen, K. L. (1987). Megaregolith insulation, internal temperatures, and bulk uranium content of the Moon. *Journal of Geophysical Research*, *92*, 3453–3465. https://doi.org/10.1029/JB092iB05p03453

White, D. R., Jongenelen, C. L., & Saunders, P. (2010). The hysteresis characteristics of some industrial PRTs. *International Journal of Thermophysics*, *31*, 1676–1684. https://doi.org/10.1007/s10765-010-0821-x

Yamazawa, K., Anso, K., Widiatmo, J. V., Tamba, J., & Arai, M. (2011). Evaluation of small-sized platinum resistance thermometers with ITS-90 characteristics. *International Journal of Thermophysics*, *32*, 2397–2408. https://doi.org/10.1007/s10765-011-1040-9

Žužek, V., Batagelj, V., & Bojkovski, J. (2010). Determination of PRT hysteresis in the temperature range from −50°C to 300°C. *International Journal of Thermophysics*, *31*, 1771–1778. https://doi.org/10.1007/s10765-010-0823-8